# Charged Higgs boson search at the Fermilab Tevatron upgrade using $\tau$ polarization

Sreerup Raychaudhuri and D. P. Roy*
*Theoretical Physics Group, Tata Institute of Fundamental Research, Homi Bhabha Road, Bombay 400 005, India*
(Received 7 March 1995)

We explore the prospect of a charged Higgs boson search in top quark decay at the Fermilab-Tevatron collider upgrade, taking advantage of the opposite states of $\tau$ polarization resulting from the $H^{\pm}$ and $W^{\pm}$ decays. Methods of distinguishing the two contributions in the inclusive one-prong hadronic decay channel of $\tau$ are suggested. The resulting signature and discovery limit of $H^{\pm}$ are presented for the Tevatron upgrade as well as the Tevatron* and the DiTevatron options.

PACS number(s): 14.80.Cp, 13.85.Qk, 13.88.+e, 14.60.Fg

## I. INTRODUCTION

There is indirect evidence for the existence of the top quark in the mass region of

$$m_t \simeq 175 \text{ GeV} \tag{1}$$

from the precision measurements of electroweak parameters, particularly at the CERN $e^+e^-$ collider LEP [1]. Moreover, a promising top quark signal in this mass range has been recently observed by the Collider Detector at Fermilab (CDF) and $D0$ Collaborations [2] at the Tevatron $\bar{p}p$ collider. The ongoing Tevatron collider experiments by the CDF and $D0$ collaborations are accumulating a luminosity of $\sim 100$ pb$^{-1}$ each, which is expected to yield a few tens of top quark events for the mass range of (1). Thus one expects to see a more definitive signal of top quark production from these experiments at the end of this run. The upgrade of the Tevatron collider luminosity via the installation of the main injector following this run is scheduled to give a typical accumulated luminosity of

$$\int \mathcal{L}\, dt \sim 2 \text{ fb}^{-1}, \tag{2}$$

which corresponds to several hundred top quark events for the above mentioned mass range (1). This will enable us to search for new particles in top quark decay; the large top quark mass offers the possibility of carrying on this search to a hitherto unexplored mass range for these particles. There has been a good deal of recent interest in the search for one such new particle, for which the top quark decay provides by far the best discovery limit [3,4]. This is the charged Higgs boson of the two-Higgs-doublet models and in particular the minimal supersymmetric standard model (MSSM).

Generally the charged Higgs boson signature in top quark decay is based on its preferential coupling to the $\tau$ channel vis-à-vis $e$ and $\mu$, in contrast with the universal $W$ coupling to all the three channels. Thus a departure from the universality prediction between these decay channels can be used to separate the charged Higgs boson signal from the $W$ boson background in

$$t \to bH(W) \to b\tau\nu. \tag{3}$$

Moreover the charged Higgs boson and the $W$ boson decays lead to opposite states of $\tau$ polarization: i.e.,

$$H^- \to \tau_R^- \bar{\nu}_R,\ H^+ \to \tau_L^+ \nu_L \tag{4}$$

and

$$W^- \to \tau_L^- \bar{\nu}_R,\ W^+ \to \tau_R^+ \nu_L \tag{5}$$

which can be used to augment the above signature (or even as an independent signature) [5, 6]. The present work is devoted to a quantitative analysis of the signature and discovery limit of the charged Higgs boson at the Tevatron upgrade based on the above ideas. In particular it shows how the $\tau$ polarization effect can be exploited to improve the signature and the discovery limit of the charged Higgs boson even without identifying the mesonic states in $\tau$ decay, which will be the case at a hadron collider.

## II. CHARGED HIGGS SIGNAL IN TOP QUARK DECAY

We shall concentrate on the charged Higgs boson of the MSSM. Its couplings to fermions are given by

$$\begin{aligned}\mathcal{L} = \frac{g}{\sqrt{2}m_W} H^+ \{ &\cot\beta\ V_{ij} m_{u_i} \bar{u}_i d_{jL} \\ &+ \tan\beta\ V_{ij} m_{d_j} \bar{u}_i d_{jR} \\ &+ \tan\beta\ m_{\ell_j} \bar{\nu}_j \ell_{jR} \} + \text{H.c.},\end{aligned} \tag{6}$$

where $V_{ij}$ are the Kobayashi-Maskawa (KM) matrix elements and $\tan\beta$ is the ratio of the vacuum expectation values of the two Higgs doublets. The QCD corrections are taken into account in the leading log approximation by substituting the quark mass parameters by their running masses evaluated at the $H^{\pm}$ mass scale [4]. Perturbative limits on the $tbH$ Yukawa couplings of Eq. (6), along with the constraints from the low-energy processes such as $b \to s\gamma$ and $B_d - \bar{B}_d$ mixing, imply the limits [7]

$$0.4 < \tan\beta < 120. \tag{7}$$

*Electronic address: dproy@theory.tifr.res.in

 

In the most predictive form of MSSM, characterized by a common supersymmetry- (SUSY-) breaking mass term at the grand unification point, one gets stronger limits [8]

$$1 < \tan\beta < m_t/m_b. \tag{8}$$

Such a lower bound also follows from requiring the perturbative limit on the $tbH$ Yukawa coupling to hold up to the unification point [9].

In the diagonal KM matrix approximation, one gets the decay widths

$$\Gamma_{t\to bW} = \frac{g^2}{64\pi m_W^2 m_t}\lambda^{\frac{1}{2}}\left(1,\frac{m_b^2}{m_t^2},\frac{m_W^2}{m_t^2}\right) \times\left[m_W^2(m_t^2+m_b^2)+(m_t^2-m_b^2)^2-2m_W^4\right], \tag{9}$$

$$\Gamma_{t\to bH} = \frac{g^2}{64\pi m_W^2 m_t}\lambda^{\frac{1}{2}}\left(1,\frac{m_b^2}{m_t^2},\frac{m_H^2}{m_t^2}\right) \times[(m_t^2\cot^2\beta+m_b^2\tan^2\beta)(m_t^2+m_b^2-m_H^2) -4m_t^2m_b^2], \tag{10}$$

$$\Gamma_{H\to\tau\nu} = \frac{g^2 m_H}{32\pi m_W^2} m_\tau^2\tan^2\beta, \tag{11}$$

$$\Gamma_{H\to c\bar{s}} = \frac{3g^2 m_H}{32\pi m_W^2}\left(m_c^2\cot^2\beta+m_s^2\tan^2\beta\right). \tag{12}$$

From these one can construct the relevant branching fractions

$$B_{t\to bH} = \Gamma_{t\to bH}/\left(\Gamma_{t\to bH}+\Gamma_{t\to bW}\right), \tag{13}$$

$$B_{H\to\tau\nu} = \Gamma_{H\to\tau\nu}/\left(\Gamma_{H\to\tau\nu}+\Gamma_{H\to c\bar{s}}\right). \tag{14}$$

It is the product of these two branching fractions that controls the size of the observable charged Higgs signal. The $t\to bH$ branching fraction has a pronounced dip at

$$\tan\beta = (m_t/m_b)^{\frac{1}{2}} \simeq 6, \tag{15}$$

where (10) has a minimum. Although this is partly compensated by a large value of the $H\to\tau\nu$ branching fraction, which is $\simeq 1$ for $\tan\beta > 2$, the product still has a significant dip at (15). Consequently the predicted charged Higgs signal will be very weak around this point as we shall see below.

The basic process of interest is $t\bar{t}$ pair production through gluon-gluon (or quark-antiquark) fusion followed by their decay into charged Higgs or $W$ boson channels: i.e.,

$$gg\to t\bar{t}\to b\bar{b}(H^+H^-, H^\pm W^\mp, W^+W^-). \tag{16}$$

The $\tau$ decay (4,5) of one or both the charged bosons leads to a single $\tau$, $\tau\tau$, or $\ell\tau$ final state, where $\ell$ denotes $e$ and $\mu$. Each of these final states is accompanied by a large missing $E_T$ and several hadronic jets.

A brief discussion of the $\tau$ identification at hadron colliders is in order here. Starting with a missing-$E_T$ trigger, the UA1, UA2, and CDF experiments have been able to identify $\tau$ as a narrow jet in its hadronic decay mode [10, 11]. In particular the CDF experiment has used the narrow jet cut to reduce the QCD jet background by an order of magnitude while retaining most of the hadronic $\tau$ events. Moreover, since the hadronic $\tau$ and QCD jet events dominantly populate the one-prong and multiprong channels, respectively, the prong distribution of the narrow jets can be used to distinguish the two. This way the CDF experiment [11] has been able to identify the $W\to\tau\nu$ events and test $W$ universality as well as put modest constraints on $t$ and $H^\pm$ masses from (3) using a data sample of integrated luminosity $\sim 4$ pb$^{-1}$. In the present case, however, one would be looking for a few tens of hadronic $\tau$ events in a data sample of $\sim 500$ times larger integrated luminosity, for which the QCD jet background cannot be controlled by the above method. Therefore one cannot use the single $\tau$ channel for the charged Higgs search and even the $\tau\tau$ channel may be at best marginal. The best charged Higgs signature is provided by the $\ell\tau$ channel. The largest background comes from $W\to\ell\nu$ accompanied by QCD jets, which can be easily suppressed by the above mentioned jet angle and multiplicity cuts. Moreover the hard isolated lepton $\ell$ provides a more robust trigger than the missing $E_T$. Therefore in this work we shall concentrate mainly on the $\ell\tau$ channel; but similar analysis can be carried over in the $\tau\tau$ channel as well.

The $\ell\tau$ and $\tau\tau$ channels correspond to the leptonic decay of both the charged bosons in (16): i.e.,

$$\begin{array}{cccccccccccc} H^+ & H^- & , & H^+ & W^- & , & H^- & W^+ & , & W^+ & & W^- \\ \downarrow & \downarrow & & \downarrow & \downarrow & & \downarrow & \downarrow & & \downarrow & & \downarrow \\ \tau_L^+ & \tau_R^- & & \tau_L^+ & \tau_L^-,\ell^- & & \tau_R^- & \tau_R^+,\ell^+ & & \tau_R^+,\ell^+ & & \tau_L^-,\ell^-. \end{array} \tag{17}$$

By convention,

$$P_\tau \equiv P_{\tau^-} = -P_{\tau^+}, \quad P_{\tau^\pm} = \frac{\sigma_{\tau_R^\pm}-\sigma_{\tau_L^\pm}}{\sigma_{\tau_R^\pm}+\sigma_{\tau_L^\pm}}. \tag{18}$$

For the $\ell\tau$ channel of our interest the signal and the background come from the $HW$ and $WW$ terms, respectively. They correspond to exactly opposite states of $\tau$ polarization: i.e.,

$$P_\tau^H = +1, \quad P_\tau^W = -1. \tag{19}$$

Consequently the use of the $\tau$ polarization effect for enhancing the signal to background ratio is particularly simple in this case as we shall see below. It may be noted here that the $\tau\tau$ channel has a better signal to background ratio because of the $HH$ contribution as well as the enhancement of $WH$ relative to $WW$ by a combinatorial factor of 2. On the other hand, the polarization distinction is less clean. While both the $\tau$'s in the background have negative polarization one or both of them have positive polarization in the signal. Nonetheless the method of enhancing the signal to background ratio by the $\tau$ polarization effect discussed below can be extended to this channel, provided one can identify the $\tau\tau$ events from the QCD background.

## III. $\tau$ POLARIZATION EFFECT

We shall concentrate on the one-prong hadronic decay channel of $\tau$, which is best suited for $\tau$ identification. It accounts for 80% of hadronic $\tau$ decays and 50% of overall $\tau$ decays. The main contributors to the one-prong hadronic $\tau$ decay are [1]

$$\tau^{\pm} \to \pi^{\pm}\nu_{\tau} \ (12.5\%), \tag{20}$$

$$\tau^{\pm} \to \rho^{\pm}\nu_{\tau} \to \pi^{\pm}\pi^{0}\nu_{\tau} \ (24\%) \ , \tag{21}$$

$$\tau^{\pm} \to a_1^{\pm}\nu \to \pi^{\pm}\pi^{0}\pi^{0}\nu_{\tau} \ (7.5\%) \ , \tag{22}$$

where the branching fractions for the $\pi$ and $\rho$ channels include the small contributions from the $K$ and $K^{\star}$ channels, respectively, since they have identical polarization effects. Note that only half the $a_1$ decay channel contributes to the one-prong configuration. The masses and widths of $\rho$ and $a_1$ are [1]

$$m_{\rho}(\Gamma_{\rho}) = 770(150) \text{ MeV}, \quad m_{a_1}(\Gamma_{a_1}) = 1260(400) \text{ MeV}. \tag{23}$$

One sees that the three decay processes (20)–(22) account for about 90% of the one-prong hadronic decay of $\tau$. Thus the inclusion of $\tau$ polarization effect in these processes will account for its effect in the inclusive one-prong hadronic decay channel to a good approximation.

The formalism relating $\tau$ polarization to the momentum distribution of its decay particles in (20)–(22) has been widely discussed in the literature [5, 6, 12, 13]. We shall only discuss the main formulas relevant for our analysis. A more detailed account can be found in a recent paper by Bullock, Hagiwara, and Martin [6], which we shall closely follow. For $\tau$ decay into $\pi$ or a vector meson $(\rho, a_1)$, one has

$$\frac{1}{\Gamma_{\pi}}\frac{d\Gamma_{\pi}}{d\cos\theta} = \frac{1}{2}(1 + P_{\tau}\cos\theta) \ , \tag{24}$$

$$\frac{1}{\Gamma_{v}}\frac{d\Gamma_{vL}}{d\cos\theta} = \frac{\frac{1}{2}m_{\tau}^2}{m_{\tau}^2 + 2m_{v}^2}(1 + P_{\tau}\cos\theta) \ , \tag{25}$$

$$\frac{1}{\Gamma_{v}}\frac{d\Gamma_{vT}}{d\cos\theta} = \frac{m_{v}^2}{m_{\tau}^2 + 2m_{v}^2}(1 - P_{\tau}\cos\theta) \ , \tag{26}$$

where $v$ stands for the vector meson and $L, T$ denote its longitudinal and transverse polarization states. The angle $\theta$ measures the direction of the meson in the $\tau$ rest frame relative to the $\tau$ line of flight, which defines its polarization axis. It is related to the fraction $x$ of the $\tau$ energy momentum carried by the meson in the laboratory frame: i.e.,

$$\cos\theta = \frac{2x - 1 - m_{\pi,v}^2/m_{\tau}^2}{1 - m_{\pi,v}^2/m_{\tau}^2}. \tag{27}$$

Here we have made the collinear approximation $m_{\tau} \ll p_{\tau}$, where all the decay products emerge along the $\tau$ line of flight in the laboratory frame.

The above distribution (24)–(26) can be simply understood in terms of angular momentum conservation. For $\tau^{-}_{R(L)} \to \nu_L \ \pi^{-}$, $v^{-}_{\lambda=0}$ it favors forward (backward) emission of $\pi$ or longitudinal vector meson, while it is the other way round for transverse vector meson emission $\tau^{-}_{R(L)} \to \nu_L v^{-}_{\lambda=-1}$. Thus the $\pi^{\pm}$'s coming from $H^{\pm}$ and $W^{\pm}$ decays peak at $x = 1$ and 0, respectively, and $\langle x_{\pi}\rangle_H = 2\langle x_{\pi}\rangle_W = 2/3$. Although the clear separation between the signal and the background peaks disappears after convolution with the $\tau$ momentum, the relative size of the average $\pi$ momenta remains unaffected: i.e.,

$$\langle p_{\pi}^{T}\rangle_H \simeq 2\langle p_{\pi}^{T}\rangle_W \ \text{ for } m_H \simeq m_W. \tag{28}$$

Thus the $\tau$ polarization effect (24) is reflected in a significantly harder $\pi^{\pm}$ momentum distribution for the charged Higgs signal compared to the $W$ boson background. The same is true for the longitudinal vector mesons; but the presence of the transverse component dilutes the polarization effect in the vector meson momentum distribution by a factor [see Eqs. (25) and (26)]

$$\frac{m_{\tau}^2 - 2m_{v}^2}{m_{\tau}^2 + 2m_{v}^2}. \tag{29}$$

Consequently the effect of $\tau$ polarization is reduced by a factor of $\sim 1/2$ in $\rho$ momentum distribution and practically washed out in the case of $a_1$. Thus the inclusive one-prong $\tau$ jet resulting from (20)–(22) is expected to be harder for the $H^{\pm}$ signal compared to the $W$ boson background; but the presence of the transverse $\rho$ and $a_1$ contributions makes the size of this difference rather modest. We shall see below that it is possible to suppress the transverse $\rho$ and $a_1$ contributions and enhance the difference between the signal and the background in the one-prong hadronic $\tau$ channel even without identifying the individual mesonic contributions to this channel.

The key feature of vector meson decay, relevant for the above purpose, is the correlation between its state of polarization and the energy sharing among the decay pions. In order to use this feature, one must first transform the polarization states of the vector meson appearing in (25) and (26) from the $\tau$ rest frame to the laboratory frame. This is done by a Wigner rotation of the vector meson spin quantization axis [14]: i.e.,

$$M'_{\lambda_{\tau}\lambda'_{v}} = \sum_{\lambda_{v}} d^{1}_{\lambda'_{v}\lambda_{v}}(\omega) M_{\lambda_{\tau}\lambda_{v}} \ , \tag{30}$$

where the decay helicity amplitudes on the left and right correspond to the laboratory and the $\tau$ rest frames, respectively, and

$$\cos\omega = \frac{(m_{\tau}^2 - m_{v}^2) + (m_{\tau}^2 + m_{v}^2)\cos\theta}{(m_{\tau}^2 + m_{v}^2) + (m_{\tau}^2 - m_{v}^2)\cos\theta} \tag{31}$$

in the collinear approximation. It may be noted that over most of the range of $\cos\theta$ the angle $\omega$ remains very small for $\rho$ and to a lesser extent for $a_1$ as well. Thus the longitudinal and transverse states of the vector meson polarization in the $\tau$ rest frame roughly correspond to those in the laboratory frame, so that the suppression of the transverse state in the latter frame corresponds to its suppression in the former as well. Using (30) and (31)

one can rewrite the decay formulas (25) and (26) in terms of the polarization states in the laboratory frame: i.e.,

$$\frac{1}{\Gamma_v}\frac{d\Gamma_{vL}^{\rm lab}}{d\cos\theta} = \frac{\frac{1}{2}m_v^2}{m_\tau^2+2m_v^2}\left[\sin^2\omega + \frac{m_\tau^2}{m_v^2}\cos^2\omega + P_\tau\cos\theta \times\left(\frac{m_\tau}{m_v}\sin 2\omega\tan\theta + \frac{m_\tau^2}{m_v^2}\cos^2\omega - \sin^2\omega\right)\right], \tag{32}$$

$$\frac{1}{\Gamma_v}\frac{d\Gamma_{vT}^{\rm lab}}{d\cos\theta} = \frac{\frac{1}{2}m_v^2}{m_\tau^2+2m_v^2}\left[1+\cos^2\omega + \frac{m_\tau^2}{m_v^2}\sin^2\omega + P_\tau\cos\theta\left(\frac{m_\tau^2}{m_v^2}\sin^2\omega - \frac{m_\tau}{m_v}\sin 2\omega\tan\theta - \cos^2\omega - 1\right)\right]. \tag{33}$$

To take account of the width of the vector meson, (32) and (33) are averaged over the vector resonance shape function [6]:

$$F_v(m^2) = \left(1-\frac{m^2}{m_\tau^2}\right)^2\left(1+\frac{2m^2}{m_\tau^2}\right)|D_v(m^2)|^2 f_v(m^2)\ , \tag{34}$$

where

$$D_v(m^2) = \frac{1}{m^2 - m_v^2 + im\Gamma_v(m^2)} \tag{35}$$

is the vector meson propagator with invariant mass $m^2$ and the running width

$$\Gamma_v(m^2) = \Gamma_v\frac{m}{m_v}\frac{f_v(m^2)}{f_v(m_v^2)}. \tag{36}$$

The $\rho$ meson line shape factor is

$$f_\rho(m^2) = (1-4m_\pi^2/m^2)^{3/2}\ , \tag{37}$$

which takes account of the $P$-wave threshold behavior for $\rho\to\pi\pi$ decay. For the line shape of the $a_1$ meson we shall use the phenomenological parametrization of Kuhn and Santamaria [15]:

$$f_a(m^2) = 1.623 + \frac{10.38}{m^2} - \frac{9.32}{m^4} + \frac{0.65}{m^6}. \tag{38}$$

The $\rho^\pm\to\pi^\pm\pi^0$ decay distributions for the two polarization states of (32) and (33) are given by

$$\frac{1}{\Gamma_{\pi\pi}}\frac{d\Gamma(\rho_L^\pm\to\pi^\pm\pi^0)}{d\cos\theta'} = \frac{3}{2}\cos^2\theta' \simeq \frac{3}{2}(2x'-1)^2\ , \tag{39}$$

$$\frac{1}{\Gamma_{\pi\pi}}\frac{d\Gamma(\rho_T^\pm\to\pi^\pm\pi^0)}{d\cos\theta'} = \frac{3}{4}\sin^2\theta' \simeq 3x'(1-x')\ , \tag{40}$$

$$x' = \left[1+\sqrt{1-4m_\pi^2/m_\rho^2}\cos\theta'\right]/2\ , \tag{41}$$

where $\theta'$ is the angle of the pion pair in the $\rho$ rest frame measured relative to the $\rho$ line of flight in the laboratory frame, and $x'$ is the fraction of the $\rho$ energy momentum carried by one of the pions (the charged one, say) in the laboratory frame. Thus $\rho_T$ decay favors equipartition of its laboratory energy between the two pions, while $\rho_L$ decay favors the asymmetric configurations where one of the pions carries all or none of its energy.

The $a_1$ decays dominantly via $\rho$; i.e.,

$$a_1^\pm\to\rho^\pm\pi^0\to\pi_1^\pm\pi_2^0\pi_3^0 \tag{42}$$

gives the one-prong decay of our interest. However, one cannot, in general, predict the energy distribution among the three pions coming from $a_{1L}$ or $a_{1T}$ decay, since each will contain $\rho_L$ and $\rho_T$ contributions with unknown relative strength. So one has to assume a dynamical model. We shall follow the model of Kuhn and Santamaria, based on the chiral limit (conserved axial vector current approximation), which provides a good description of the $a_1\to 3\pi$ data [15]. In this model the decay amplitude is given by

$$M = \epsilon_\nu^{T,L}J^\nu(a_1^\pm\to\pi_1^0\pi_2^0\pi_3^\pm)\ , \tag{43}$$

$$J^\nu \sim D_{a_1}(s)\left[D_\rho(s_{13})(\tilde p_3-\tilde p_1)^\nu + D_\rho(s_{23})(\tilde p_3-\tilde p_2)^\nu\right]\ , \tag{44}$$

$$\tilde p_i^\nu = p_i^\nu - p_{a_1}^\nu\frac{p_{a_1}\cdot p_i}{s}\ , \tag{45}$$

where $e_\nu$ is the $a_1$ polarization vector and we have dropped a constant multiplicative factor in (44), which will not be relevant for our analysis. It will be adequate for our purpose to evaluate the decay amplitudes (43)–(45) neglecting the $a_1$ and $\rho$ widths. The resulting decay distributions for longitudinal and transverse $a_1$ are given by

$$\frac{1}{\Gamma_{3\pi}}\frac{d\Gamma(a_{1L}\to 3\pi)}{d\cos\theta_a d\cos\theta_\rho d\phi_\rho} = \frac{\left[\frac{m_a^2+m_\rho^2}{m_a m_\rho}\cos\theta_a\cos\theta_\rho - 2\sin\theta_a\sin\theta_\rho\cos\phi_\rho\right]^2}{\frac{8\pi}{9}\left[\left(\frac{m_a^2+m_\rho^2}{m_a m_\rho}\right)^2+8\right]}, \tag{46}$$

$$\frac{1}{\Gamma_{3\pi}}\frac{d\Gamma(a_{1T}\to 3\pi)}{d\cos\theta_a d\cos\theta_\rho d\phi_\rho} = \frac{\left[\frac{m_a^2+m_\rho^2}{m_a m_\rho}\sin\theta_a\cos\theta_\rho + 2\cos\theta_a\sin\theta_\rho\cos\phi_\rho\right]^2 + 4\sin^2\theta_\rho\sin^2\phi_\rho}{\frac{16\pi}{9}\left[\left(\frac{m_a^2+m_\rho^2}{m_a m_\rho}\right)^2+8\right]}. \tag{47}$$

In the $a_1^\pm \to \rho^\pm \pi^0$ decay $\theta_a$ is the angle of $\rho$ in the $a_1$ rest frame measured relative to the $a_1$ line of flight in the laboratory ($z$ axis), while the plane containing these two vectors defines the $x$-$z$ plane. Similarly in the $\rho^\pm \to \pi^\pm \pi^0$ decay $\theta_\rho$ and $\phi_\rho$ are the polar and azimuthal angles of the charged pion in the $\rho$ rest frame, measured relative to the above $\rho$ line of flight ($z'$ axis) and the above plane, respectively. In terms of these angles, the fraction of $a_1$ laboratory energy-momentum carried by the charged pion is given by

$$\begin{aligned} x' &= \frac{E_{\pi^\pm}}{E_{a_1^\pm}} \\ &= \frac{1}{m_a}\left[\frac{m_\rho}{2}\frac{m_a^2+m_\rho^2}{2m_a m_\rho} + \frac{m_\rho}{2}\frac{m_a^2-m_\rho^2}{2m_a m_\rho}\cos\theta_a \right. \\ &\quad + q\frac{m_a^2-m_\rho^2}{2m_a m_\rho}\cos\theta_\rho + q\frac{m_a^2+m_\rho^2}{2m_a m_\rho}\cos\theta_\rho\cos\theta_a \\ &\quad \left. - q\sin\theta_\rho\cos\phi_\rho\sin\theta_a\right], \end{aligned} \tag{48}$$

$$q = \frac{1}{2}\sqrt{m_\rho^2 - 4m_\pi^2} \simeq \frac{1}{2}m_\rho. \tag{49}$$

One sees from (48) that

$$x' \simeq 1 \quad \text{for} \quad \cos\theta_a \simeq 1 \quad \text{and} \quad \cos\theta_\rho \simeq 1, \tag{50}$$

while

$$x' \simeq 0 \quad \text{for} \quad \cos\theta_a \simeq -1 \quad \text{or} \quad \cos\theta_\rho \simeq -1. \tag{51}$$

The $a_{1L}$ decay distribution (46) has maxima near

$$\cos\theta_a = \pm 1 \quad \text{along with} \quad \cos\theta_\rho = \pm 1, \tag{52}$$

which correspond to collinear decay into $3\pi$ resulting in unequal distribution of energy. This is similar to the $\rho_L^\pm \to \pi^\pm\pi^0$ decay, except that in the present case there is a visible peak only at $x' \simeq 0$ but not at $x' \simeq 1$. The reason is that the latter condition holds only for a tiny region of the phase space as we see from (50). The $a_{1T}$ decay distribution (47) vanishes near the collinear configuration (52). It has maxima at

$$\cos\theta_a = 0 \quad \text{and} \quad \cos\theta_\rho = \pm 1 \quad \text{or} \quad \cos\theta_\rho = 0, \quad \cos\phi_\rho = 0 \tag{53}$$

which correspond to the plane of the three decay pions in the $a_1$ rest frame being normal to its line of flight. This results in an even sharing of the $a_1$ energy as in the case of $\rho_T$ decay. In particular both the distributions vanish at the extrema $x' = 0$ and 1 and peak near the middle, although the $a_{1T}$ peak occurs a little below $x' = 0.5$. Indeed the shapes of $a_{1L}$ and $a_{1T}$ decay distributions in $x'$ are qualitatively similar to those of $\rho_L$ and $\rho_T$, except for the suppression of the $x' \simeq 1$ peak for $a_{1L}$. A comparison of these distributions can be found in [6]. There is reason to believe that the above features of longitudinal and transverse $a_1$ decay are insensitive to the assumed dynamical model [15]. Indeed it follows from general considerations that the $a_{1L(T)} \to 3\pi$ decay favors the plane of the three pions in the $a_1$ rest frame being coincident with (normal to) the $a_1$ line of flight [13]. The role of the model is only to determine the distribution of energy among the three pions in this plane. Moreover, as shown in [6], the alternative model of Isgur *et al.* [16] gives very similar pion energy distributions as that of [15].

Thus the transverse $\rho$ and $a_1$ decays favor even sharing of energy by the charged and neutral pions, while the longitudinal $\rho$ and $a_1$ decays favor extreme configurations where the charged pion carries practically all or none of the vector meson energy. This can be exploited to suppress the former while retaining most of the latter contributions along with that of the pion (20). This will in turn enhance the $H^\pm$ signal to $W^\pm$ background ratio in the one-prong hadronic decay channel of $\tau$ as we shall see below.

## IV. RESULTS AND DISCUSSION

We shall be interested in the inclusive one-prong hadronic decay of $\tau$, which is dominated by the $\pi^\pm, \rho^\pm$, and $a_1^\pm$ contribution (20)–(22). It results in a thin one-prong hadronic jet ($\tau$ jet) consisting of a charged pion along with 0, 1, or 2 $\pi^0$'s, respectively. Since all the pions emerge in a collinear configuration one can neither measure their invariant mass nor the number of $\pi^0$'s. Consequently it is not possible to identify the mesonic state. But it is possible to measure the energy of the charged track as well as the total neutral energy, either by measuring the momentum of the former in the central detector and the total energy deposit in the electromagnetic (EM) and hadron calorimeters or from the showering profiles in the EM and hadron calorimeters. Thus one has to develop a strategy to suppress the transverse vector meson contributions using these two pieces of information. We shall consider two such strategies below. In either case a rapidity and transverse energy cut of

$$|\eta| < 2 \quad \text{and} \quad E_T > 20 \text{ GeV} \tag{54}$$

will be applied on the $\tau$ jet (as well as the lepton $l$), where $E_T$ includes the neutral contribution. We shall use the recent structure functions of [17] for calculating the $t\bar{t}$ cross section.

First, we consider the effect of an isolation cut requiring the neutral $E_T$ accompanying the charged track within a cone of $\Delta R = (\Delta\eta^2 + \Delta\phi^2)^{1/2} = 0.2$ to be

$$E_T^{\text{ac}} \equiv E_T^0 < 5 \text{ GeV}. \tag{55}$$

Figure 1 shows the $E_T^{\text{ac}}$ distribution for a $\tau$ jet satisfying (54). The $\pi$, $\rho$, and $a_1$ contributions are shown separately for the $H^\pm$ signal and the $W^\pm$ background, where we have chosen $m_H = 80$ GeV and $\tan\beta = 1$ for illustrative purpose. The $\bar{p}p$ c.m. energy is taken to be 2 TeV. Several points are worth noting in this figure.

(i) The signal to background ratio for $\pi$ ($\sim 4.5$) is twice as large as $\rho$ and thrice as large as $a_1$. This is a consequence of the $E_T > 20$ GeV cut and the $\tau$ polarization effect (24)–(29).

(ii) The $\rho$ and $a_1$ contributions to the signal (background) are dominated by the longitudinal (transverse) components.

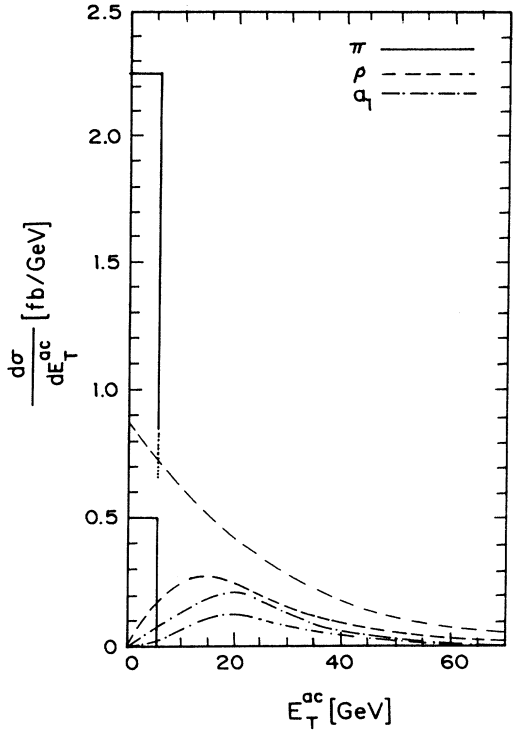


FIG. 1. The $\pi^{\pm}, \rho^{\pm}$, and $a_1^{\pm}$ contributions to the one-prong hadronic $\tau$-jet cross section coming from the $H^{\pm}$ signal (upper curves) and $W^{\pm}$ background (lower curves) for $m_H =$ 80 GeV and $\tan\beta = 1$ at $\sqrt{s} = 2$ TeV. The cross sections are shown as functions of neutral pion $E_T$ accompanying the charged track in the $\tau$ jet.

(iii) The $\rho_L^{\pm} \to \pi^{\pm}\pi^0$ peak at $x' \simeq 1$ shows up in the signal at $E_T^{ac} \simeq 0$ while the $x' \simeq 0$ peak is smeared over the large $E_T^{ac}$ tail. The absence of a $E_T^{ac} \simeq 0$ peak in the $a_{1L}^{+} \to \pi^{\pm}\pi^0\pi^0$ contribution to the signal reflects the absence of a corresponding peak at $x' \simeq 1$ as remarked earlier, while the $x' \simeq 0$ peak is smeared over the large $E_T^{ac}$ tail.

(iv) The $\rho_T^{\pm} \to \pi^{\pm}\pi^0$ peak at $x' \simeq 0.5$ shows up in the background at $E_T^{ac} \simeq 15$ GeV. The peak in the $a_{1T}^{\pm} \to \pi^{\pm}\pi^0\pi^0$ contribution to the background at a somewhat higher $E_T^{ac}$ reflects the corresponding peak at $x'$ somewhat below 0.5 as remarked earlier.

As one sees from Fig. 1, the isolation cut (55) on the charged track will essentially remove all the contributions except for $\pi^{\pm}$ and a part of the $\rho_L^{\pm} \to \pi^{\pm}\pi^0$ corresponding to its $x' \simeq 1$ peak, where the decay $\pi^0$ is very soft. Consequently the signal to background ratio is enhanced by a factor of $\sim 2$; but the signal size goes down by a factor of $\sim 2.5$. Of course the enhancement of the signal to background ratio increases further with increasing $E_T$ cut as we shall see below. Moreover, the isolation cut has the advantage of suppressing the QCD jet background. Nonetheless the factor of 2.5 drop in the signal size is a high price to pay, particularly at the Tevatron collider [18]. The reason for this big drop in the signal size is of course that the isolation cut removes not only the $\rho_T$ and $a_{1T}$ contributions but also large parts of the $\rho_L$ and $a_{1L}$ contributions corresponding to their $x' \simeq 0$ peaks. The second strategy discussed below aims at retaining these latter contributions.

Here one plots the rate of $\tau$-jet events, satisfying (54), as a function of

$$\Delta E_T = |E_T^{ch} - E_T^0| = |E_T^{ch} - E_T^{ac}|; \tag{56}$$

i.e., the difference between the $E_T$ of the charged track and the accompanying neutral $E_T$. The hard $\tau$-jet events from the $H^{\pm}$ signal and $W^{\pm}$ background are expected to be dominated by the $\pi, \rho_L, a_{1L}$ and the $\rho_T, a_{1T}$ contributions, respectively. The latter contributions favor comparable values of $E_T^{ch}$ and $E_T^0$ and hence relatively small $\Delta E_T$, while the former favor large values of $\Delta E_T$. Thus the signal events are expected to show significantly harder $\Delta E_T$ distribution compared to the background.

Figure 2 shows the $\tau$-jet cross sections from the $H^{\pm}$ signal and the $W^{\pm}$ background for $\tan\beta = 1.4$ and two values of $H^{\pm}$ mass, viz. 100 and 140 GeV.

Figures 2(a) and 2(b) show the $E_T$ distributions of the inclusive one-prong $\tau$ jet events from (20)–(22) be-

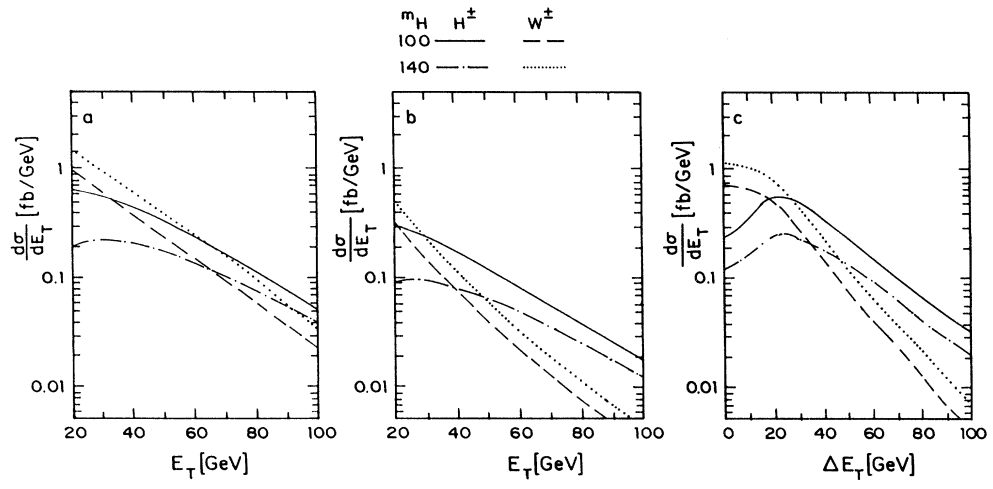


FIG. 2. The one-prong hadronic $\tau$-jet cross sections are plotted against the jet $E_T$ in (a) without and (b) with the isolation cut. They are plotted against the $\Delta E_T$ of the jet in (c). The $H^{\pm}$ signal ($W^{\pm}$ background) contributions are shown as solid (dashed) lines for $m_H = 100$ GeV and dot-dashed (dotted) lines for $m_H =$ 140 GeV. We take $\sqrt{s} = 2$ TeV and $\tan\beta = 1.4$.

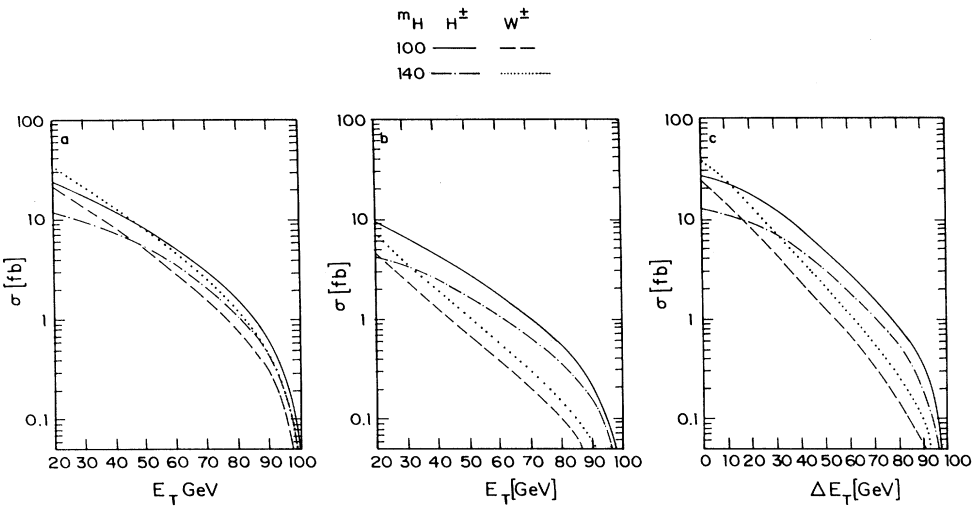


FIG. 3. The integrals of the signal and background cross sections of Figs. 2(a)–2(c) shown against the cutoff $E_T$ ($\Delta E_T$). The legend of the curves are the same as in Fig. 2.

fore and after the isolation cut (55). The isolation cut is clearly seen to enhance the signal to background ratio, but at the cost of a drop in the signal size. The signal to background ratio improves by a factor of 1.5–3 over the $E_T$ range shown, while the signal size drops by a factor of 2–3. Figure 2(c) shows these inclusive one-prong $\tau$-jet events as a function of $\Delta E_T$. Evidently the signal events have a much harder $\Delta E_T$ distribution than the background, which is far more striking than the difference in the corresponding $E_T$ distributions shown in Fig. 1(a). Thus the $\Delta E_T$ distribution provides a much clearer separation between the signal and the background than the simple $E_T$ distribution. It helps to improve the signal to background ratio significantly without sacrificing the signal size.

Figure 3 shows the corresponding integrated cross sections against the cutoff value of the $E_T(\Delta E_T)$: i.e.,

$$\sigma(E_T) = \int_{\infty}^{E_T} \frac{d\sigma}{dE_T} dE_T. \tag{57}$$

These plots are well suited for comparing the relative merits of the three methods in extracting the signal from the background. For this purpose the cutoff values are to be so chosen that one gets a viable

$$H^\pm \text{ signal}/W^\pm \text{ background} \geq 1. \tag{58}$$

The resulting signal size is a reasonable criterion for the merit of the method. Comparing the signal and background cross sections for $m_H = 140$ GeV, we see that this condition is achieved at a far greater sacrifice to the signal size in Fig. 3(a) than in 3(b) and 3(c). The size of the resulting signals, as given by the corresponding crossover points, are $\sim 1/2$ fb, 3 fb, and 7 fb, respectively. Making a similar comparison of the signal and background cross sections for $m_H = 100$ GeV, one sees that the ratio 1 is reached in Fig. 3(a) with a signal size of $\sim 2$ fb, which is larger than that in 3(b) and comparable to the one in 3(c). However, the ratio increases more rapidly with cutoff in the latter two cases compared to the first. Since this increase is required to offset the rapid fall of the signal to background ratio with increasing $\tan\beta$ [see Eqs. (9) and (10)], the latter methods give more favorable signal size at $\tan\beta > 1.4$ as shown in Fig. 4.

Figures 4(a)–4(c) show the size of the signals from the three methods satisfying a viable signal to background ratio $> 1$. The signal cross sections are shown as functions of $\tan\beta$ for $m_H = 80$, 100, 120, and 140 GeV. One clearly sees that the use of $\tau$ polarization effect via the

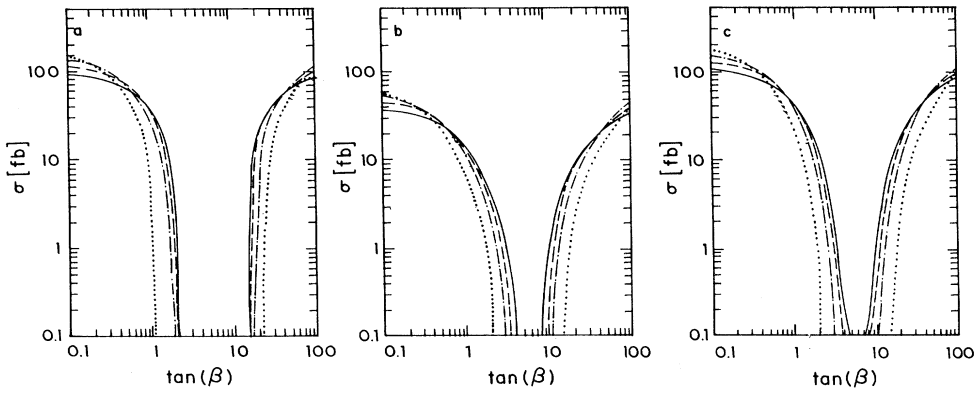


FIG. 4. The signal cross section of Figs. 3(a)–3(c), satisfying a signal to background ratio $\geq 1$, are shown as functions of $\tan\beta$ for $m_H = 80$, 100, 120, and 140 GeV by solid, dashed, dot-dashed, and dotted lines, respectively.

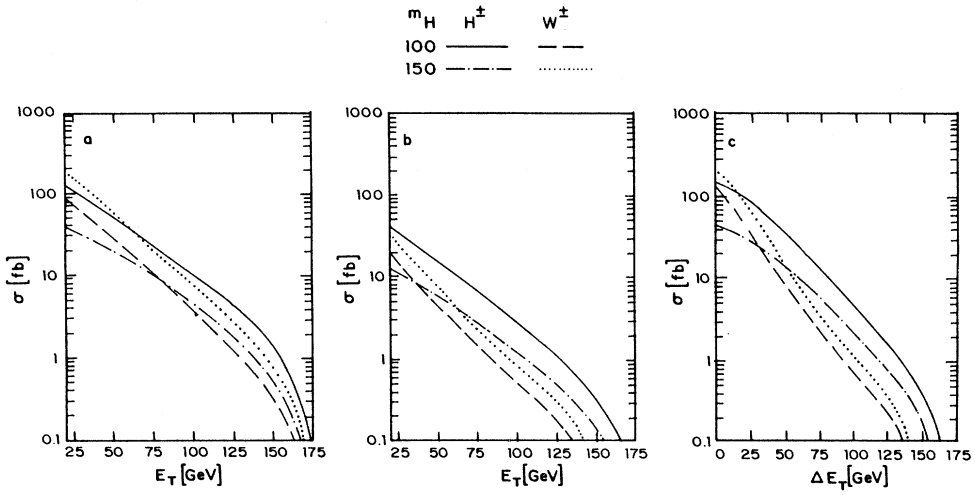


FIG. 5. The integrals of the signal and background cross sections are shown against cutoff $E_T$ ($\Delta E_T$) as in Fig. 3, but for $\sqrt{s} = 4$ TeV. The solid (dashed) and dot-dashed (dotted) lines correspond to the signal (background) for $m_H = 100$ and 150 GeV, respectively. We take $\tan\beta = 1.4$.

isolation cut [Fig. 4(b)] or the $\Delta E_T$ distribution [Fig. 4(c)] will give a viable charged Higgs signal over a wider range of the charged Higgs boson mass and $\tan\beta$ parameters.

It is reasonable to consider a signal size of 10 fb, satisfying a signal to background ratio $\geq 1$, to constitute a viable charged Higgs signal. With the expected integrated luminosity of $\sim 2$ fb$^{-1}$, this will correspond to 20 signal events over a $W$ boson background of similar size. Since the number of background events can be predicted from the number of dilepton ($\ell^+\ell^-$) events in $t\bar{t}$ decay using $W$ universality, this will correspond to a 4.5 $\sigma$ signal for the charged Higgs boson. Thus one can get the discovery limit of charged Higgs boson at the Tevatron upgrade by demanding a signal size of 10 fb in Fig. 4. Evidently the best limits come from Fig. 4(c). For $m_H = 100$ (120) GeV one expects a viable signal except for the region $\tan\beta = 2$–15 (1.5–20). The gap in the $\tan\beta$ space is due to the dip in the $t \to bH$ coupling at $\tan\beta \sim 6$, as remarked before. It may be mentioned here that there is a current suggestion of further upgradation of Tevatron luminosity by another order of magnitude — i.e., the Tevatron*. The corresponding discovery limit of charged Higgs boson can be obtained by demanding a signal size of 1 fb in Fig. 4(c). In this case the gap narrows down to $\tan\beta = 3$–10 (2.5–12) for $m_H = 100$ (120) GeV. Moreover one can probe for $m_H = 140$ GeV except for a gap in the region $\tan\beta = 2 - 15$.

For the sake of completeness we have computed the signal and background cross sections for the suggested DiTevatron energy of $\sqrt{s} = 4$ TeV. Figure 5 shows the integrated signal and background cross sections against the cutoff $E_T$ ($\Delta E_T$) analogous to Fig. 3 for $m_H = 100$ and 150 GeV. The curves are very similar to those of Fig. 3 except for a factor of $\sim 4$ increase in normalization. Figure 6 shows the signal cross sections, satisfying signal to background ratio $\geq 1$, as functions of $\tan\beta$ for $m_H = 80, 100, 120, 140$, and 150 GeV. Comparing Figs. 4 and 6 one sees better discovery limit at the DiTevatron for comparable luminosity. It should be noted, however, that the signal cross section of $\sim 10$ fb at the DiTevatron has similar contours in the $m_H$ and $\tan\beta$ space as that of $\sim 1$ fb at the Tevatron. Thus one expects similar discovery limits for charged Higgs boson at the DiTevatron and the Tevatron*. In either case there remains a gap near $\tan\beta \sim 6$, so that the nonobservation of a signal will not rule out the presence of a charged Higgs boson in the 100–140 GeV region unambiguously.

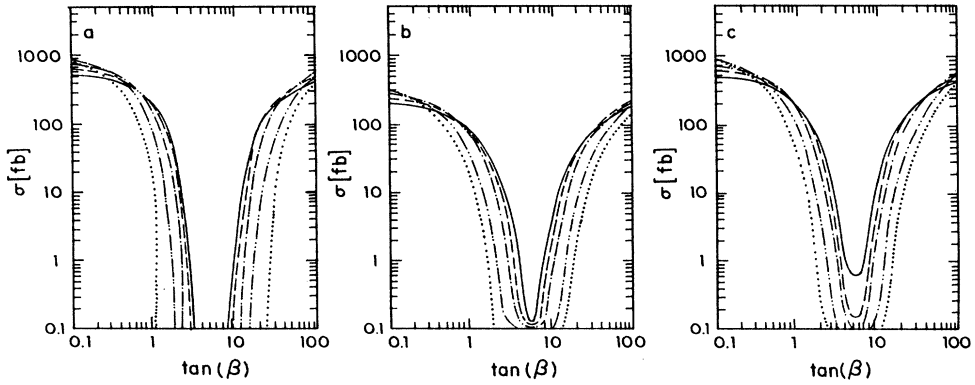


FIG. 6. The signal cross sections of Figs. 5(a)–5(c), satisfying a signal to background ratio $\geq 1$, are shown as functions of $\tan\beta$ for $m_H = 80, 100, 120, 140$, and 150 GeV by solid, dashed, dot-dashed, double-dot-dashed, and dotted lines, respectively.

## V. SUMMARY

We have explored the prospect of charged Higgs boson search in top quark decay at the Tevatron collider upgrade, taking advantage of the opposite states of $\tau$ polarization resulting from the $H^{\pm}$ and $W^{\pm}$ decays. We have concentrated on the decay of $\tau$ into a one-prong hadronic jet ($\tau$ jet), which is dominated by the $\pi^{\pm}, \rho^{\pm}$, and $a_1^{\pm}$ mesons. The positive (negative) polarization of $\tau$ coming from the $H^{\pm}$ signal ($W^{\pm}$ background) is shown to favor unequal (equal) sharing of the $\tau$-jet energy between the charged prong ($\pi^{\pm}$) and the accompanying neutral pions. Consequently the two polarization states can be distinguished by measuring the charged and neutral contributions to the one-prong $\tau$-jet energy even without identifying the individual meson states. We have shown how this can be used for better separation of the charged Higgs signal from the $W$ boson background. In particular we have considered two strategies—(1) an isolation cut on the $\tau$-jet events requiring the neutral contribution to the jet transverse energy to be small ($E_T^0 < 5$ GeV), and (2) a redistribution of the $\tau$-jet events in $\Delta E_T$, i.e., the difference between the charged and neutral contributions to the jet $E_T$ instead of their sum. In either case one gets a substantial enhancement in the signal to background ratio. But this is accomplished at the cost of a reduction in the signal size in the first case, while there is no such price to pay in the second. Consequently, the latter strategy offers the best discovery limit for the charged Higgs boson. We have explored these discovery limits in the parameter space of $H^{\pm}$ mass and $\tan\beta$ assuming an integrated luminosity of $\sim 2$ fb$^{-1}$ for the Tevatron upgrade. For the sake of completeness we have also explored the signal and discovery limit for the suggested Tevatron* and DiTevatron options, corresponding to an order of magnitude increase of luminosity and a doubling of the c.m. energy, respectively.

## ACKNOWLEDGMENTS

It is a pleasure to thank R. M. Godbole, N. K. Mondal, and Probir Roy for discussions. The work of S.R. was partially supported by a project (DO No. SR/SY/P-08/92) of the Department of Science and Technology, Government of India.

[1] Particle Data Group, L. Montanet *et al.*, Phys. Rev. D **50**, 1173 (1994).

[2] CDF Collaboration, F. Abe *et al.*, Phys. Rev. Lett. **73**, 225 (1994); Phys. Rev. D **50**, 2966 (1994); Phys. Rev. Lett. **74**, 2626 (1995); *D*0 Collaboration, S. Abachi *et al.*, *ibid.* **74**, 2632 (1995).

[3] V. Barger and R.J.N. Phillips, Phys. Rev. D **41**, 884 (1990); A.C. Bawa, C.S. Kim, and A.D. Martin, Z. Phys. C **47**, 75 (1990); R.M. Godbole and D.P. Roy, Phys. Rev. D **43**, 3640 (1991).

[4] M. Drees and D.P. Roy, Phys. Lett. B **269**, 155 (1991); D.P. Roy, *ibid.* **283**, 403 (1992).

[5] R.M. Barnett *et al.*, in *Research Directions for the Decade*, Proceedings of the Summer Study, Snowmass, Colorado, 1990, edited by E.L. Berger (World Scientific, Singapore, 1991); B.K. Bullock, K. Hagiwara, and A.D. Martin, Phys. Rev. Lett. **67**, 3055 (1991); D.P. Roy, Phys. Lett. B **277**, 183 (1992).

[6] B.K. Bullock, K. Hagiwara, and A.D. Martin, Nucl. Phys. **B395**, 499 (1993).

[7] V. Barger, J.L. Hewett, and R.J.N. Phillips, Phys. Rev. D **41**, 3421 (1990); J.F. Gunion and B. Grzadkowski, Phys. Lett. B **243**, 301 (1990); A.J. Buras *et al.*, Nucl. Phys. **B337**, 284 (1990).

[8] G. Ridolfi, G.G. Ross, and F. Zwirner, in *Proceedings of the ECFA Large Hadron Collider Workshop*, Aachen, many, 1990, edited by G. Jarlskog and D. Rein (CERN Report No. 90-10, Geneva, Switzerland, 1990), Vol. II, p. 608.

[9] J. Bagger, S. Dimopoulos, and E. Masso, Phys. Rev. Lett. **55**, 920 (1985).

[10] UA2 Collaboration, J. Alitti *et al.*, Phys. Lett. B **280**, 137 (1992); UA1 Collaboration, C. Albajar *et al.*, *ibid.* **251**, 459 (1991).

[11] CDF Collaboration, F. Abe *et al.*, Phys. Rev. Lett. **72**, 1977 (1994).

[12] Y.S. Tsai, Phys. Rev. D **4**, 2821 (1971); P. Aurenche and R. Kinnunen, Z. Phys. C **28**, 261 (1985); K. Hagiwara, A.D. Martin, and D. Zeppenfeld, Phys. Lett. B **235**, 198 (1990).

[13] A. Rouge, Z. Phys. C **48**, 75 (1990).

[14] See, e.g., A.D. Martin and T.D. Spearman, *Elementary Particle Theory* (North-Holland, Amsterdam, 1970), p. 321.

[15] J.H. Kuhn and A. Santamaria, Z. Phys. C **48**, 445 (1990).

[16] N. Isgur, C. Morningstar, and C. Reader, Phys. Rev. D **39**, 1357 (1989).

[17] A.D. Martin, R.G. Roberts, and W.J. Sterling, Phys. Lett. B **306**, 145 (1993); **309**, 492 (1993).

[18] The isolation cut strategy may be more appropriate at the CERN Large Hadron Collider, where the signal size is very large.